Biomedical Signal Processing and Control 89 (2024) 105802

Contents lists available at ScienceDirect

Biomedical Signal Processing and Control

journal homepage: www.elsevier.com/locate/bspc

A general framework for the assessment of scatter correction techniques in digital mammography

Francesca Angelone [a,1], Alfonso Maria Ponsiglione [a,*,1], Roberto Grassi [b], Francesco Amato [a,2], Mario Sansone [a,2]

[a] Department of Electrical Engineering and Information Technology, University of Naples 'Federico II', Naples, Italy
[b] Department of Precision Medicine Division of Radiology, University of Campania 'Luigi Vanvitelli', Naples, Italy

ARTICLE INFO

Keywords:
Breast imaging
PSF modeling
Scatter correction
X-ray scattering

ABSTRACT

Scattered radiation negatively impacts radiographic imaging, with particular regard to mammography. In clinical practice, anti-scatter grids are exploited for this purpose; however, anti-scatter grids may also degrade the image quality, since they remove part of the useful primary radiation with the consequent increase of the dose to be administered to the patient. A suitable digital scatter correction method could tackle the limits imposed by such grids with a great impact on diagnosis. The main contribution of this study is the development of a general framework for the assessment of digital scatter correction techniques in mammography. To this aim, the formation process of both primary and scattered image is described on the basis of a systems-theory approach. Through a simulation of the radiological process, a reference model of the primary image is obtained and used as ground truth to compare the intensities of images obtained by applying a deconvolution-based digital scattering correction technique. Then, an experimental case study on breast phantom images is carried out to assess the scatter correction using different Point Spread Functions (PSFs) (Gaussian and Hyperbolic) with varying parameters values. A central issue was the identification of a spatially variant PSF to model the scattered radiation. The results demonstrate that the proposed approach enables the assessment and the comparison of different PSF kernels employed for scatter correction; in particular, our procedure shows that rather low relative errors are obtained ([−0.5;0.5]) for both the PSFs tested and that Gaussian ones are more sensitive to variations in their parameters.

1. Introduction

Soft tissue imaging, such as breast imaging, is greatly affected by the scatter phenomenon. To make accurate diagnoses it is therefore important to develop methods that aim to improve the quality of mammography images by removing the scatter component. The literature has suggested a variety of methods to enhance the quality of medical images, e.g by means of contrast enhancers [1–4], or by applying post-processing techniques based on Artificial Intelligence (AI) algorithms [5–11], or, like in the case of digital mammography, by the use of an anti-scatter grid.

The latter, however, has the disadvantage of cutting primary radiation components, which are fundamental for image formation process, with the consequent need for increased X-ray dose to achieve adequate image quality [12]. Furthermore, the anti-scatter grid is not able to completely remove the scattered radiation and, as a result, the breast image obtained is still affected by the detrimental effect of the scattering phenomenon. Therefore, methods for digital scatter removal become necessary in digital mammography also to overcome the main limitations of anti-scatter grids. Among the scatter removal approaches in X-ray imaging, convolution-based filtration techniques are widely employed in the literature.

Shaw et al. [13] and Love and Kruger [14] applied a digital correction based on convolution to digital subtraction angiography (DSA) for different purposes; the former developed a videodensitometry system, the latter showed that two-dimensional exponential kernels best reproduced the scatter fields. Subsequently, Molloi and Mistretta [15] tried to correct the scattering and veiling glare phenomena using Gaussian convolution kernels. Naimuddin et al. [16] studied a scatter correction method using a convolution algorithm with variable weighting to improve the scatter estimate and provide better results

* Corresponding author.
E-mail address: alfonsomaria.ponsiglione@unina.it (A.M. Ponsiglione).
[1] F.A. and A.M.P. contributed equally to this work.
[2] F.A. and M.S. contributed equally to this work.

https://doi.org/10.1016/j.bspc.2023.105802
Received 31 March 2023; Received in revised form 19 November 2023; Accepted 25 November 2023
Available online 5 December 2023

for general videodensitometric applications. Floyd et al. [17] presented a numerical deconvolution technique to compensate image degrading effects in X-ray chest images using Fourier deconvolution. Kruger et al. [18] showed that dual-kernel algorithms are more effective than equivalent single-kernel algorithms. In the digital mammography field, Baydush and Floyd [19] studied the effect of bayesian image estimation on digital mammograms to reduce the scatter content and improve the contrast-to-noise ratio. Furthermore, a number of research studies examined the application of spread functions [20] and digital filtering [21–23] to study the scattering phenomena.

Based on the existing literature, in-depth knowledge and understanding of the X-ray scattering phenomenon and how it affects the acquired mammograms are required in order to build adequate image processing approaches for the accurate removal of the scattering. Basically, the scatter effect occurring within an X-ray Image Intensifier (XRII), i.e. a device that converts an incident X-ray pattern to a visible-light image [24], can be described as a linear process. Indeed, Seibert et al. (1984) [25] originally attempted to derive a theoretical model of the so-called veiling glare, a term used to describe the scattering of electrons and light photons within an XRII. They were able to derive the analytical expression of the Point Spread Function (PSF) of an XRII based on three fundamental assumptions on the scattering process and on the PSF behavior:

1. linearity;
2. spatial invariance;
3. independence on X-ray energy.

They made the case of an accelerated electron striking an infinitely thin and uniform phosphor material of a typical XRII. Starting from the above-mentioned assumptions and by equating the net flow of scattered photons through the area of the phosphor material to the total energy in the same area [25], they derived a theoretical model of the phenomenon which was then adapted to digital mammography by Ducote and Molloi [26]. The key premise of the model is that the incoming radiation is represented as a pencil beam that grows predictably after it enters the tissues, mimicking the dispersed radiation.

Taking advantage of the current knowledge on the scattering phenomenon and on previous studies [27], this work proposes a general framework for the assessment of the scatter correction in mammograms. The studies present in the literature on the scattering phenomenon propose an evaluation based either on theoretical knowledge on the diagnostic aspects of interest [13,14] or they calculate the error in the estimation of the scatter kernel with respect to direct physical measurements made with a phantom relating to specific organs [15,17]. In the approach we propose, by exploiting a system theory approach, a theoretical model of the imaging process is defined and some related research questions are proposed. Our procedure is then applied to a case study aimed at assessing the scatter correction techniques proposed in the literature. We shall start from the assumption established in earlier works, which suggested modeling the scatter radiation using a radially symmetric PSF representing the interaction between the main radiation and the tissues being studied. We shall focus, therefore, on the optimization of the suitable shape for the PSF that models the scattering phenomenon, and a modeling strategy based on the use of a classical Gaussian PSF and an hyperbolic PSF as proposed by Ducote and Molloi [26], will be adopted.

In particular, the methodological workflow here proposed consists of a simulation approach followed by an experimental case study on mammographic images acquired on a breast phantom. In order to evaluate the accuracy of the scatter removal from the mammographic image, the radiological process is simulated to compute the theoretical and ideal primary radiation intensities. This will allow us to obtain a reference model of the image intensities in absence of the scattering phenomenon. This simulated model is then taken as ground truth to calculate the errors produced by the two PSF models with respect to the theoretical reference, and make an assessment of the scatter correction.

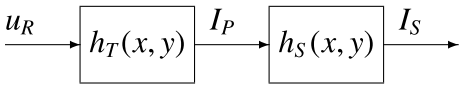

Fig. 1. Theoretical model of the image acquisition chain in the space domain.

This work will show that, thanks to the proposed framework for the assessment of digital correction techniques, it is possible to demonstrate the feasibility of the correction methods proposed in the literature and to arrive at important considerations on the scattering phenomenon. The results obtained allow us to conclude that a digital removal of the scatter is feasible and that the scatter correction is influenced by the makeup of the tissues and the thickness of the area under examination. Moreover, our study proves that a Gaussian kernel outperforms a hyperbolic kernel in minimizing the scattering component of the radiation, proving that the suggested methodology enables the assessment and the comparison of different PSF kernels employed for scatter correction.

2. Methods

2.1. Theoretical framework

Tissue–radiation interaction can be described, from a theoretical perspective, as reported in Fig. 1, where, said $\mathbb{N}$ the set of integer numbers and $(x, y) \in \mathbb{N}\times\mathbb{N}$ the coordinate of a given pixel, the involved signals are

$u_R(x, y)$ the incident radiation
$I_P(x, y)$ the primary image
$I_S(x, y)$ the scattered image

Each block in Fig. 1 is described in the space domain by the corresponding impulse response, as follows:

$h_T(x, y)$ impulse response (kernel) modeling the tissues–radiation interaction
$h_S(x, y)$ impulse response (kernel) of the scatter dynamics

The spatial convolution, between the impulse response of the block in Fig. 1 and its input, determines the output of the blocks. Note that, in this paper, we have neglected the spatial dynamics of the sensors, since, as usual, we have assumed that each pixel of the sensors panel is described as a memory-less system with unit input–output gain; indeed, in that case, the input–output gain of the whole sensors panel is invariant over space (i.e. unitary for all pair (x, y)) and its kernel function turns out to be the impulse function centered at $(0, 0)$.

Under this assumption, the output of the whole system in Fig. 1 is given by (we omit the space argument for the sake of brevity)

$$I_S = h_S * \left(h_T * u_R\right) , \tag{1}$$

where $*$ denotes the convolution operator.

From the engineering point of view, the acquisition scheme depicted in Fig. 1 leads to some problems to be solved in order to improve the image quality.

Problem 1 (*Estimation of the Primary Image*)**.** Given the scattered image $I_S(\cdot, \cdot)$, to estimate the primary image $I_P(\cdot, \cdot)$. ■

In order to solve Problem 1, we need to invert the equation

$$I_S(x, y) = h_S(x, y) * I_P(x, y),$$

through the deconvolution operator $dec(\cdot, \cdot)$

$$I_P(x, y) = dec\left(h_S(x, y), I_S(x, y)\right) . \tag{2}$$

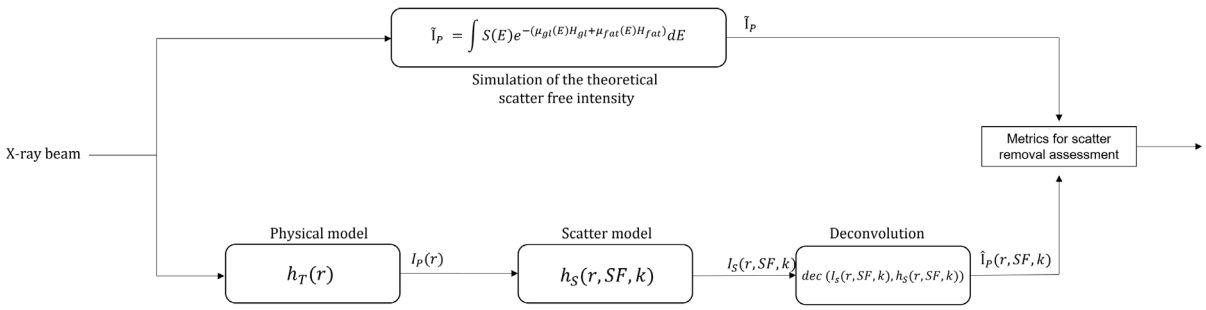

Fig. 2. Block diagram for the identification problem.

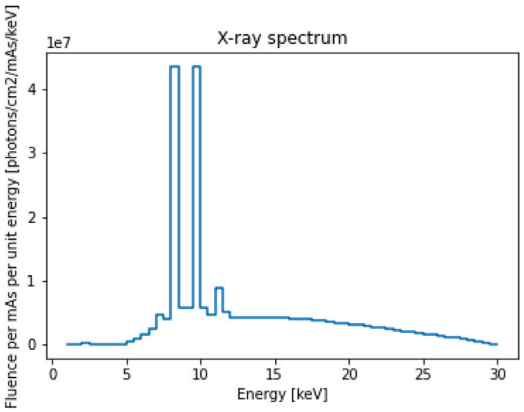

Fig. 3. X-ray spectrum at 30 kVp obtained with Spekpy tool.

Therefore, in view of (2), Problem 1 is essentially reduced to the identification of the kernel $h_S(\cdot,\cdot)$.

Regarding the scheme in Fig. 1, another problem, of great interest in the field of mammographic imaging, can be posed. In particular, when the primary image has been identified, an important issue concerns the identification of the tissue response to radiation.

Problem 2 (*Identification of the Tissue Response*)**.** Given the primary image $I_P(\cdot,\cdot)$ and the incident radiation $u_R(\cdot,\cdot)$, to identify the kernel $h_T(\cdot,\cdot)$. ■

This paper will be devoted to the solution of Problem 1, while Problem 2 and the related possible applications will be the object of future investigation. To this regard, it is worth noting that, by the solution of Problem 2, an estimated model of the response of the tissues to the incident radiation will be available, through the knowledge of h_T; such response, in turn, could be exploited to generate synthetic images, starting from different radiation inputs $u_R(x,y)$, which may have many relapses in the clinical field as envisaged in literature studies [28–30].

2.2. Primary image formation process

In order to describe the formation process of the primary image (I_P), a simulation of the radiological process was developed to simulate the intensities of a theoretical scatter-free image, $\tilde{I}_P$, representing the simulation of the theoretical I_P in the absence of scattering phenomena.

The simulation of the radiological process is described in the upper path of the scheme in Fig. 2 and is based on the computation of the theoretical intensities, using the equation:

$$\tilde{I}_P = \int S(E)\exp(-(\mu_{gl}(E)H_{gl} + \mu_{fat}(E)H_{fat}))dE\,, \tag{3}$$

where E is the energy and $S(E)$ is the spectrum of the incident radiation, which is obtained by the simulation at 30 kVp (to which the images of the phantom were acquired) using the Spekpy toolkit [31]; the behavior of $S(E)$ is showed in Fig. 3. In (3) the parameters μ_{gl} and μ_{fat} are the linear attenuation coefficients of the glandular and adipose tissues (functions of E), respectively, while H_{gl} and H_{fat} are the thickness of the glandular and adipose tissues, respectively. The linear attenuation coefficients used in (3) have been provided by the manufacturer of the phantom.

2.3. Scattered image formation process

As illustrated in Section 2.1, the scatter can be seen as the effect of low-pass 2D-convolution filtering of the primary image (I_P). Therefore, the scattered image (I_S) can be written as the convolution between the primary component and the impulse response of the scatter dynamics (h_S).

The formation process of the scattered image (I_S) is depicted in the first two blocks of the lower path of the scheme in Fig. 2, which are then followed by a deconvolution block between h_S and I_S to compute the estimated intensity of the scatter-free image, $\hat{I}_P$, representing the estimate of I_P after the digital scatter removal.

In scatter correction, the problem of noise amplification is significant, as it deteriorates the quality of the medical image, reducing the Contrast-to-noise ratio (CNR) [32,33]. In this deconvolution-based approach, this aspect has been considered through the appropriate tuning of the deconvolution operator. In particular, a damping factor deconvolution method has been used and the damping factor has been properly tuned in order to prevent the noise amplification for those pixels slightly deviating from the noise level. Furthermore, readout noise variance of the noise and additive noise have been taken into account.

In order to properly describe the scattered image formation process and to obtain more accurate estimates of I_S, the characterization and modeling of the scattering kernel h_S is crucial.

In accordance with the literature, we shall assume the radiation beam is a matrix of pencil beams, which expand in a predictable way according to the theoretical scatter phenomenon as soon as it penetrates tissues. Therefore, the total pixel value of the X-ray image is represented as the sum of both the scatter and the primary component of the radiation.

As far as the h_S model, we shall investigate two different kernel functions as illustrated in the following.

In the first case, h_S is assumed to have a Gaussian behavior with zero mean, namely:

$$h_S(x,y) \equiv h_{SG}(x,y) = (1+SF)\frac{1}{2\pi k^2}e^{-(\frac{x^2+y^2}{2k^2})}\,. \tag{4}$$

Since the scattering phenomenon modeled through (4) exhibits a radial symmetry, in the following, by a change of variable, we shall

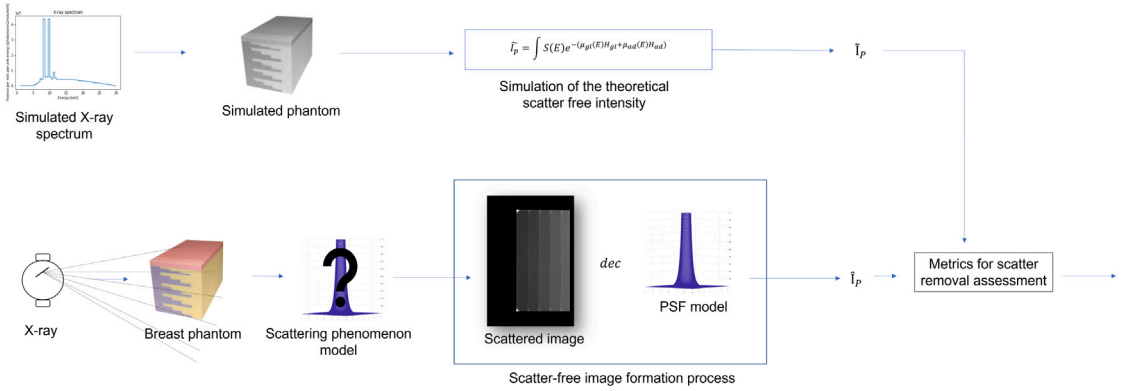

Fig. 4. Schematic representation of operative workflow. (*dec* stands for the deconvolution operator as detailed in the main text; $\hat{I}_P$ is the estimated intensity of the scatter-free image obtained by a deconvolution).

refer to kernels depending on only one variable r, where $r^2 = x^2 + y^2$, therefore we rewrite (4) as follows:

$$h_{SG}(r) = (1 + SF)\frac{1}{2\pi k^2} e^{-\left(\frac{r^2}{2k^2}\right)}. \tag{5}$$

where:

- r represents the distance from the origin (i.e. from the point where the incident accelerated electron strikes the phosphor material);
- SF represents the fraction of light that is strongly scattered, hence $0 < SF < 1$;
- $k \neq 0$ represents the mean scatter radial extent (i.e. the mean propagation distance of the light in the phosphor material).

In the second case, an alternative hyperbolic behavior for h_S, introduced by Seibert et al. in 1984 [25], is considered and defined as follows:

$$h_S(r) \equiv \tilde{h}_{SH}(r) = (1 - SF)\frac{\delta(r)}{r} + \frac{SF}{2kr} e^{-r/k}, \tag{6}$$

where:

- $1 - SF$ represents the fraction of light that is not scattered and, thereby, provides a direct mapping of the incident electron on the phosphor material;
- the impulse function centered at $r = 0$, namely $\delta(r)$, accounts for the mapping of the primary component;
- the function $\frac{1}{2kr} e^{-r/k}$ represents the spread of the energy at a distance r. This term can be derived from (7) as reported in [25]:

$$E(r) = \frac{1}{2\pi r_0 r} e^{-r/r_0}, \tag{7}$$

with r_0 being the mean diffusion distance.

The terms SF and k in (6) take into account the behavior of the scattering kernel. If Eq. (6) is normalized with respect to the non-scattered light fraction $(1 - SF)$, it can be rewritten as in (8), according to the authors of [26], who applied the PSF proposed by Seibert et al. [25] to the case of digital mammography:

$$h_{SH}(r) = \frac{\delta(r)}{r} + \frac{SF}{(1 - SF)2kr} e^{-r/k}. \tag{8}$$

It is readily seen that the behavior of both h_{SG} and h_{SH} is regulated by two parameters, namely the scatter fraction (SF) and the mean radial extension (k).

When looking at the gaussian PSF, h_{SG}, such parameter values can be interpreted as a wider, intermediate, and narrower Gaussian in terms of standard deviation.

Concerning h_{SH}, the values of SF and k have been chosen on the basis of the limits imposed by the function previously defined.

Different values of the above-mentioned scatter kernel parameters will be used and discussed in the case study illustrated in Section 2.4.

Table 1
Summary of the value of SF and k tested for h_{SG} and for h_{SH}.

	SF	k
h_{SG}	0.5	0.01
	0.99	0.001
	0.2	0.1
h_{SH}	0.5	0.01
	0.99	0.001
	0.2	0.1

2.4. Case study

An experimental case study is carried out to implement the proposed framework, as graphically illustrated in Fig. 4.

The upper path in Fig. 4 produces the simulated theoretical scatter-free image, $\tilde{I}_P$, while the lower path in Fig. 4 produces the estimated scatter-free image by the deconvolution operator discussed in Section 2.1.

The experimental campaign was carried out on digital mammography images of a breast phantom with regions of known adipose and fibroglandular tissue composition and at different thicknesses, as detailed in Section 2.5. The choice of such a structured phantom was made to investigate the effectiveness of the scatter correction evaluation approach at different breast tissues' composition, size, and thickness.

As far as the characterization of the PSF model of the scattering phenomenon, different values have been chosen for the independent parameters SF and k presented in Section 2.3. In particular, the scatter kernel parameters here tested are summarized in Table 1. These two terms control the behavior of the scatter kernel and have been studied in detail in [34]. To evaluate the behavior of the Gaussian and hyperbolic PSF, object of the case study in the paper, it was decided to consider the maximum, minimum and an intermediate value referring to the previously cited work of Leon et al. [34] where a characterization of scatter in digital mammography is done. This involves a study on a more or less significant scatter component based on the chosen values.

Finally, to evaluate the effect of the digital scatter correction, a comparison between the scatter-free images intensities by deconvolution ($\hat{I}_P$) and the simulated theoretical intensities ($\tilde{I}_P$) by Eq. (3), taken as references, was carried out.

2.5. Experimental settings

The phantom used for the acquisitions is the Mammo CESM Phantom (Sun Nuclear Corporation), described in [35]. It is made of four adipose-glandular blocks, made of High Equivalency materials accurately described in [36], with five steps of glandularity (0%, 25%, 50%, 75%, 100%) [35], with a thickness that can range from 1 to 9 cm.

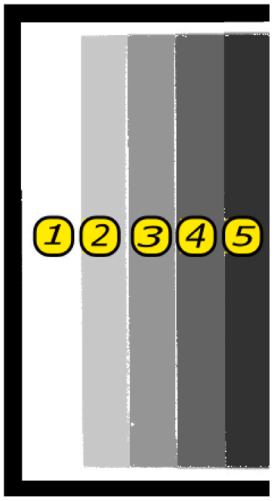

Fig. 5. Schematic representation of the phantom with the five ROI, from 1 to 5, that represent, respectively, the ROI with 100%, 75%, 50%, 25%, 0% of adipose tissue.

In Fig. 5 a schematic representation of the phantom is shown, where the five Regions of Interest (ROIs), representing the five glandularity steps, are highlighted.

Phantom mammographic images were acquired using Giotto Class (IMS GIOTTO S.p.A., Sasso Marconi, Bologna, Italy). For each thickness of the phantom (from 1 to 9 cm), 30 KVp and 100 mAs were set. The mammograph used had a tungsten anode with a 10 degree angle and used a 0.05 mm thick silver filter.

The acquisitions were made using a physical grid in accordance with the clinical protocol. The graphite interspaced antiscatter grid mounted on the Giotto Class mammograph has a grid ratio of 5:1, with a line density of 36 lines/cm and a focal distance of 68.5 cm.

Only raw acquired images ("FOR PROCESSING" images) were taken into account as they preserve the original X-ray attenuation information.

2.6. Metrics for the assessment of the scatter correction

To evaluate the accuracy of the convolution-based digital scatter correction, a comparison between the values obtained for $\tilde{I}_P$ and $\hat{I}_P$ is carried out. In particular, we considered the scatter removal satisfactory when the estimated intensity of the scatter-free image, $\hat{I}_P$, obtained by a deconvolution between the measured intensity of the scattered image I_S and the PSF h_S, is comparable to the simulated intensity of the theoretical scatter-free image, $\tilde{I}_P$. A scaling factor (here equal to 0.04), which takes into account the conversion gain of the detector and the contribution of the anti-scatter grid, is applied to yield the value of the simulated intensity of the theoretical scatter-free image, $\tilde{I}_P$ obtained in (3).

The following two different metrics were used for the assessment of the scatter correction:

- the ratio between the intensity values calculated from the available X-ray images, both scattered (I_S) and scatter-free ($\hat{I}_P$), and the simulated intensity ($\tilde{I}_P$) values, is calculated for each region of the phantom;
- the relative error, defined as the ratio between the punctual error (Err) on the primary image estimate, which is given as the difference between $\hat{I}_P$ - $\tilde{I}_P$, and the theoretical scatter-free image $\tilde{I}_P$.

Plots and heat maps were used to visualize the metrics here adopted.

3. Results and discussion

In Fig. 6, the ratio between the scattered intensities and the simulated intensities is shown; each plot in Fig. 6 is referred to a different ROI and thickness of the phantom.

In order to better analyze the behavior following the removal of the scatter, in the single ROI and in the whole phantom at the various thicknesses, the previously described error maps and relative error trend plots have been reported.

In the following, we consider three cases.

Case 1. $[h_S \equiv h_{SG}$ *with* $SF = 0.5$ *and* $k = 0.01]$

The results related to the ratio between the scatter-free and simulated intensities, as a function of the phantom ROIs, when the primary image is obtained by h_{SG}, are shown in Fig. 13(a).

Note that, in Fig. 6, the ratio between the intensity values of the scattered (measured) image and the simulated intensity, obtained through Eq. (3), varies between 0.7 and 2, without considering the background.

Conversely, as expected, removing the scatter radiation through the application of the Gaussian-type PSF, namely h_{SG}, reduced values of the ratio, ranging between 0.6 and 1.3, are obtained, as shown in Fig. 13(a). In other words, we are approaching the unit value, that

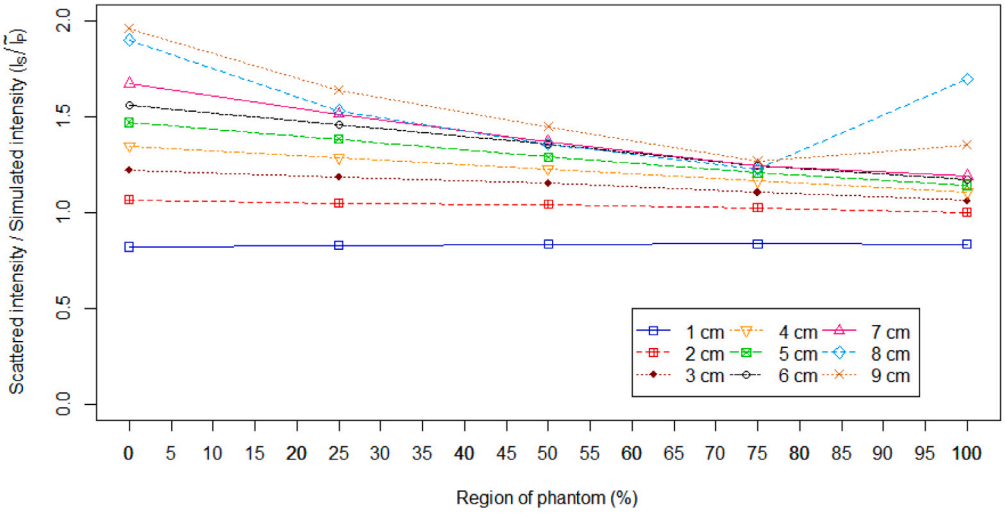

Fig. 6. Ratio between the scattered intensities and the simulated intensities for the measured image as a function of the phantom region (%).

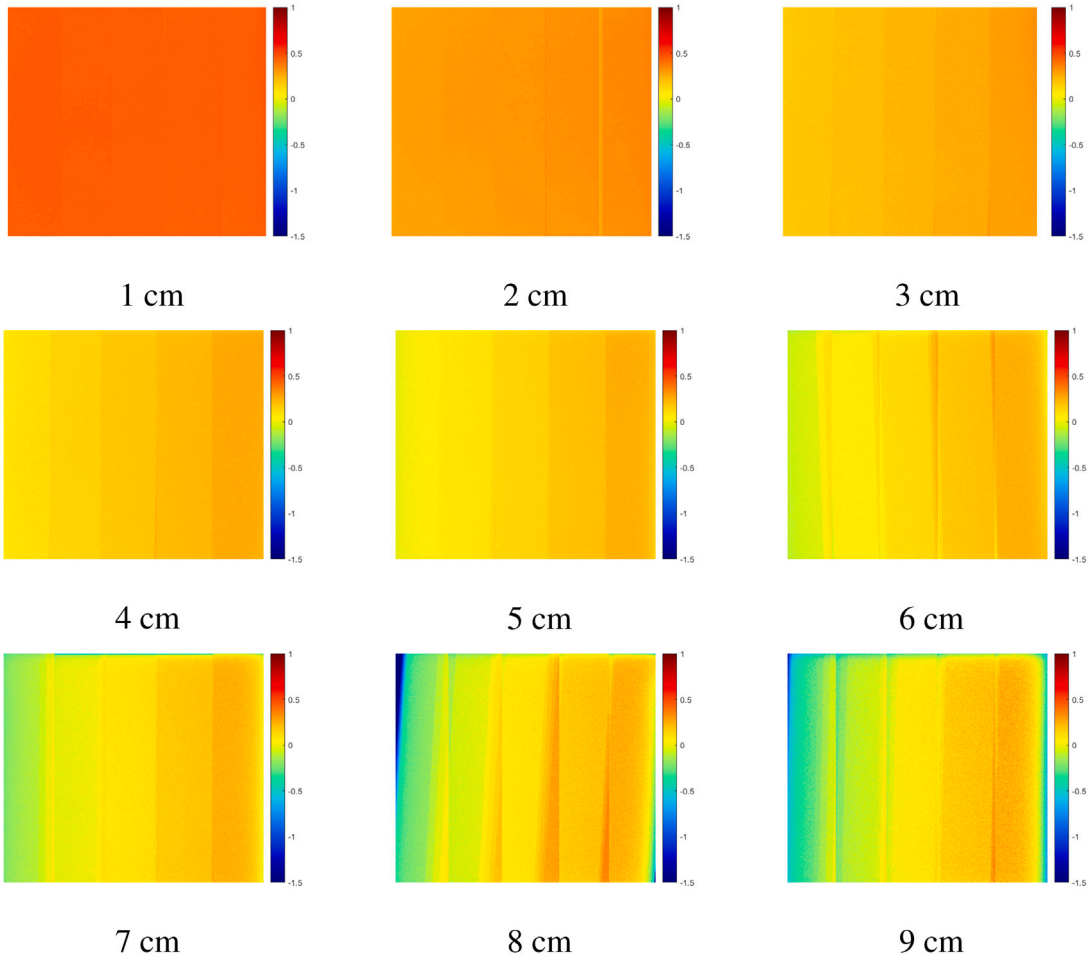

Fig. 7. Relative error distribution on five ROIs of phantom for thickness from 1 cm (top right) to 9 cm (lower left) in case 1.

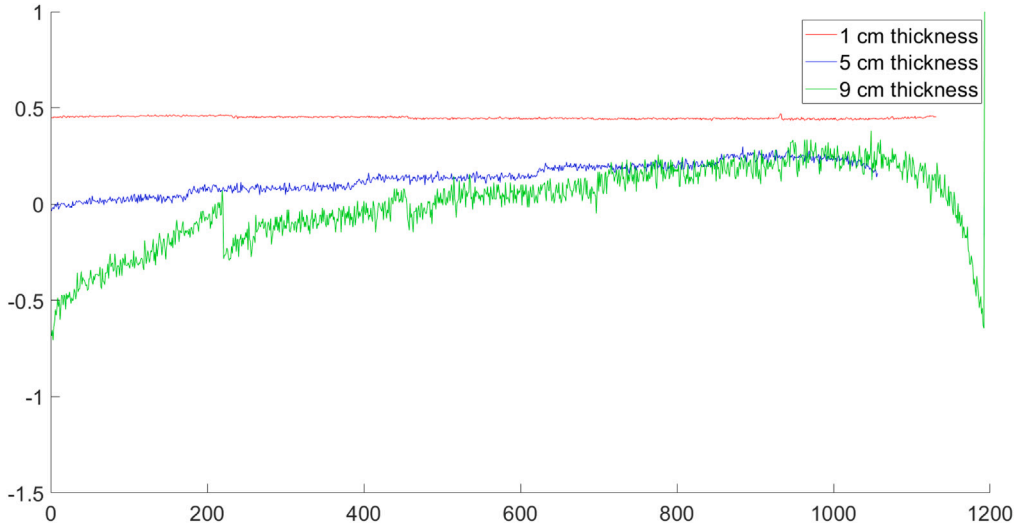

Fig. 8. Relative error trend on five ROIs of phantom for thickness 1 cm, 5 cm and 9 cm in case 1.

represents the desired target. There remains a certain variability in relation to both the thickness of the phantom and the regions and therefore to the different composition of adipose and glandular tissue.

From this discussion, it is evident the dependence of the goodness of the scatter removal on the composition of the tissues and on the thickness of the phantom.

As said, we then evaluate the relative error behavior in every single ROI.

In Fig. 7 the error distribution maps for the five phantom ROIs (from 100% fat on the left to 100% glandular on the right) for all phantom thicknesses are shown. As far as ROI 1 (100% fat) is concerned, it is possible to note that the distribution of the relative error

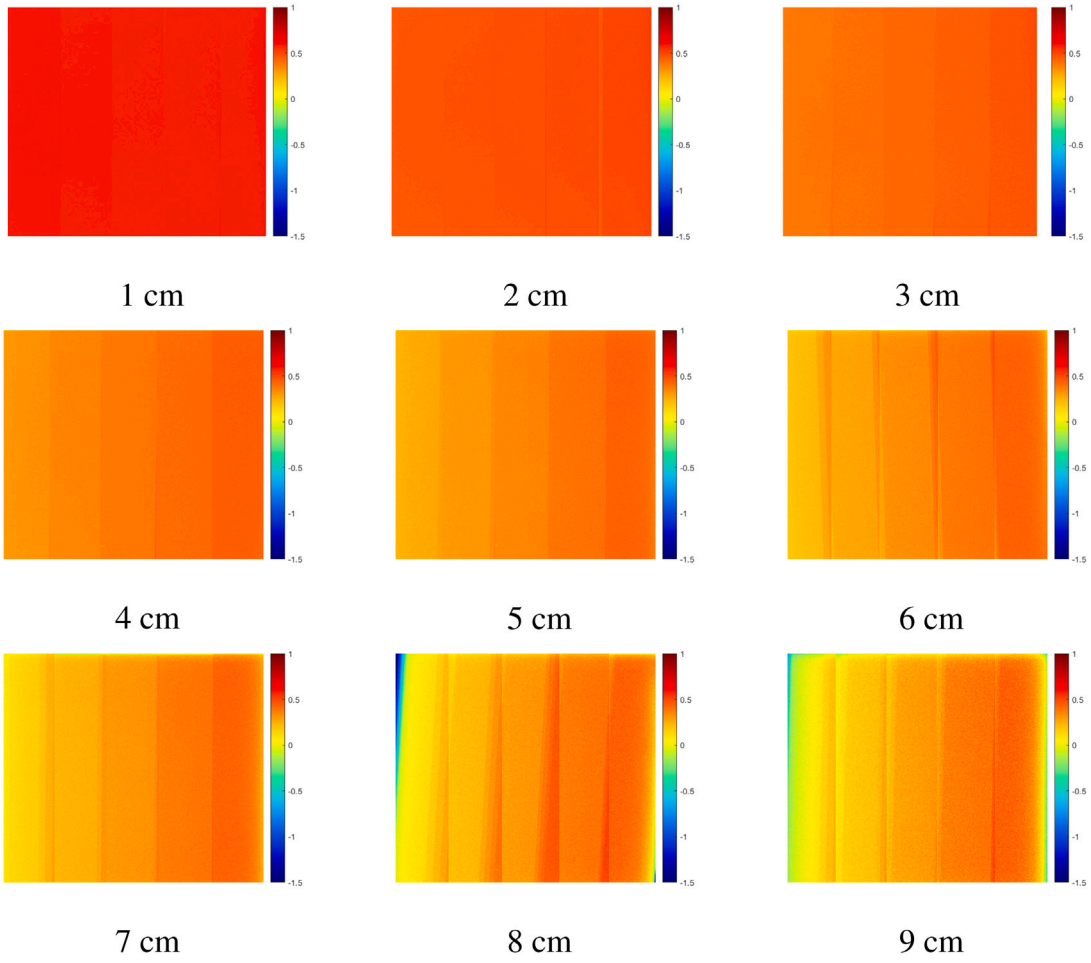

Fig. 9. Relative error distribution on five ROIs of phantom for thickness from 1 cm (top right) to 9 cm (lower left) in case 2.

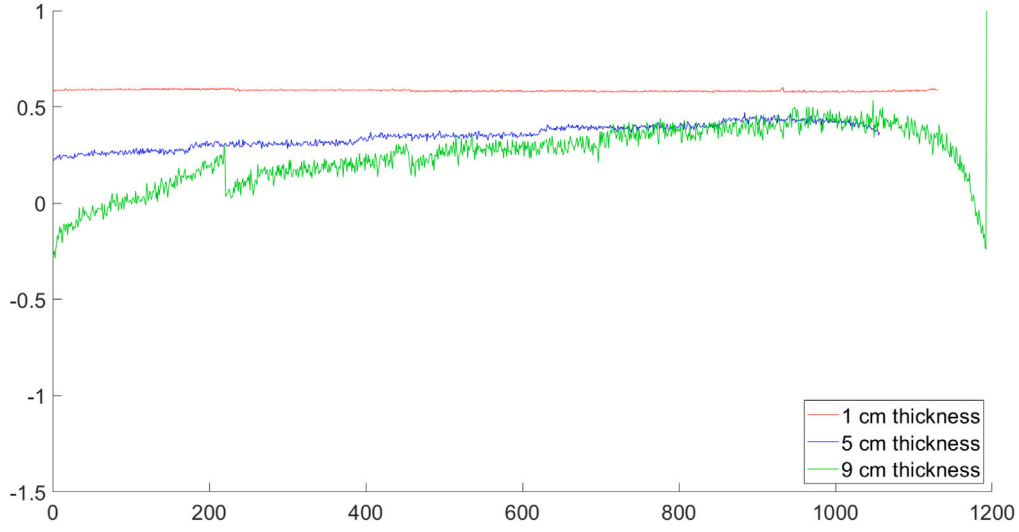

Fig. 10. Relative error trend on five ROIs of phantom for thickness 1 cm, 5 cm and 9 cm in case 2.

is homogeneous over the entire layer, especially for low thicknesses. For high thicknesses, there is an error trend that is mainly affected by the influence of the projection of the superimposed layers, and by the influence of those adjacent ROIs that have a different composition of glandular and adipose tissues. As far as ROI 5 (100% glandular) is concerned, it is possible to note that the relative error distribution is affected by an increasing noise for all thicknesses. In this case, the influence of the projection of the superimposed layers is less evident, but it is possible to see the influence of the edge effects. In this case, the mutual influence between ROIs and edge effects is highlighted.

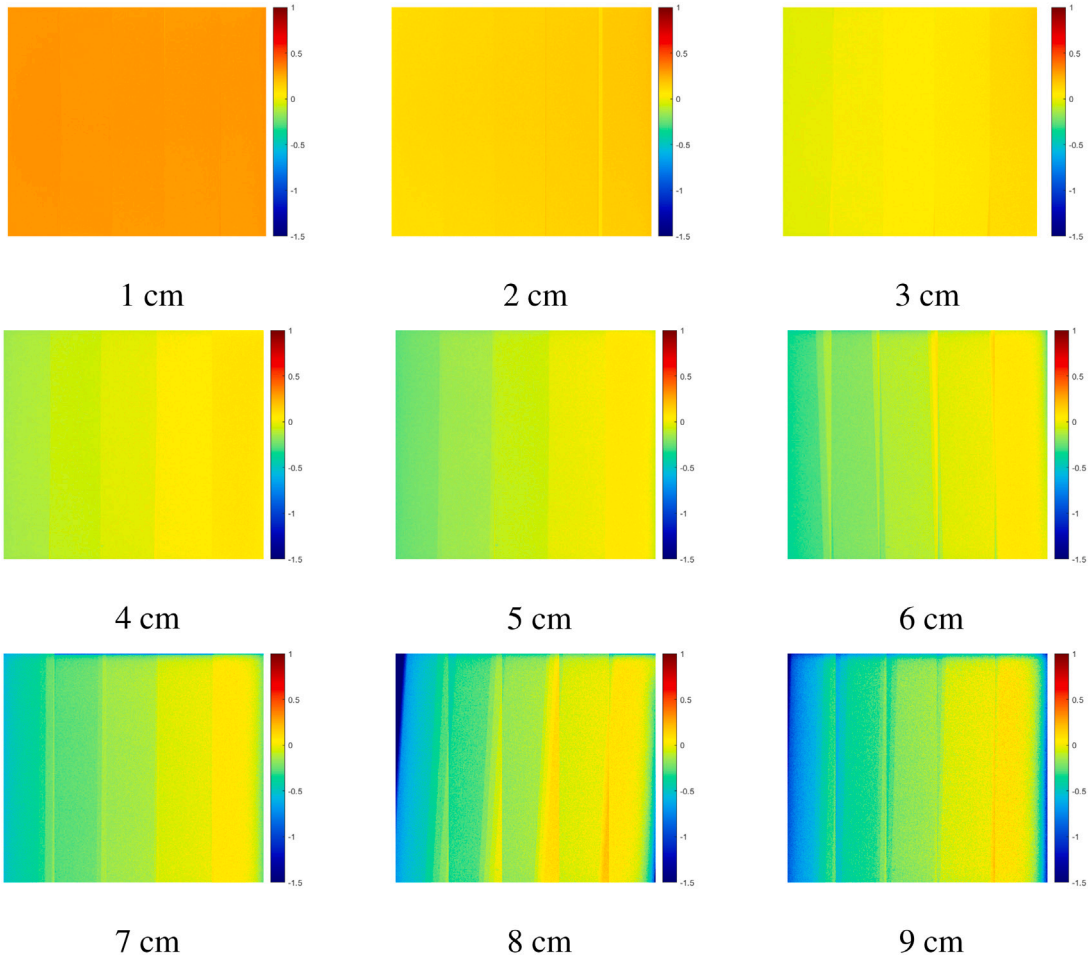

Fig. 11. Relative error distribution on five ROIs of phantom for thickness from 1 cm (top right) to 9 cm (lower left) in case 3.

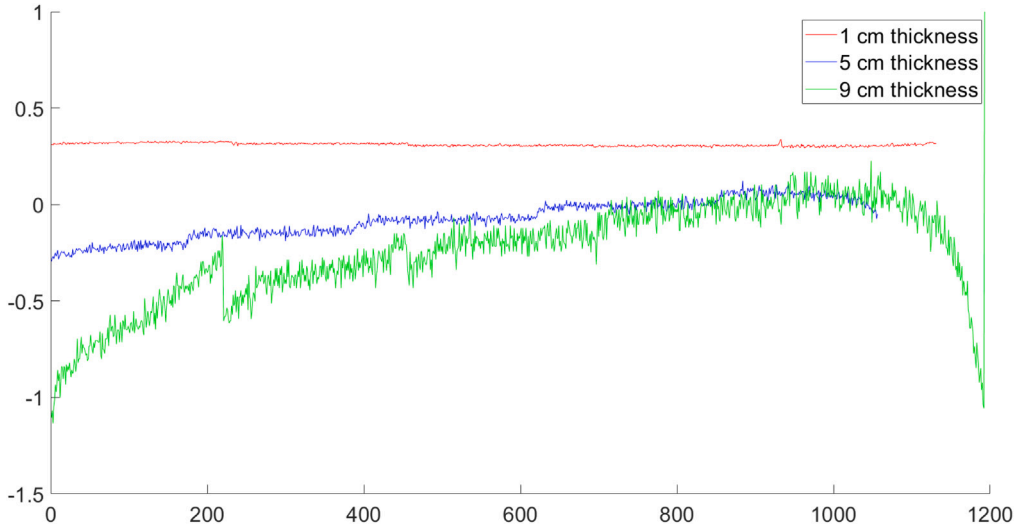

Fig. 12. Relative error trend on five ROIs of phantom for thickness 1 cm, 5 cm and 9 cm in case 3.

The same considerations can be better deduced from the graphs in Fig. 8 which show the trend of the relative error along the 5 layers of which the phantom is made up, reported for the overall thickness of the phantom of 1 cm, 5 cm and 9 cm. From here it is possible to note that the relative error remains in a range of [0;0.5], except in the 9 cm thickness where a strong component of noise on the edges and the effect of the superimposed layers is evident, as already highlighted in the errors maps.

Case 2. *[$h_S \equiv h_{SG}$ with $SF = 0.99$ and $k = 0.001$]*

In this case we are considering a Gaussian PSF with a double amplitude and a standard deviation equal to 1/10 compared to the

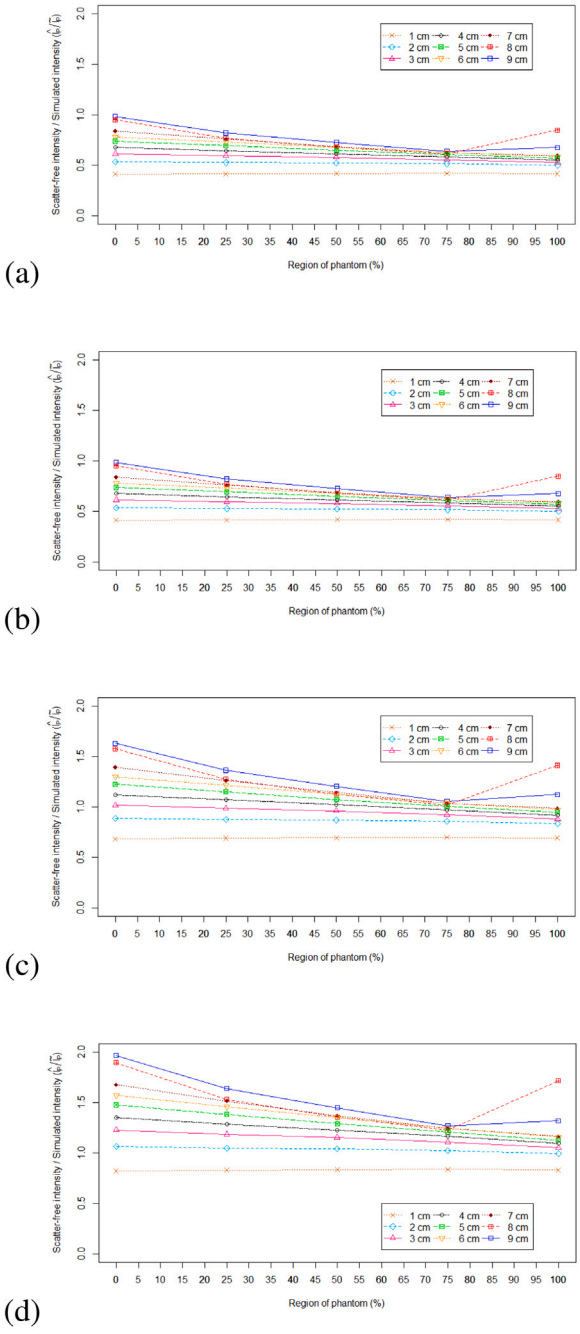

Fig. 13. Ratio between the scatter-free intensities and the simulated intensities when the primary image is calculated by h_{SG} in the case 1 *(a)*, in the case 2 *(b)*, in the case 3 *(c)* and by h_{SH} in the case 4 *(d)*, as a function of the ROI of the phantom (%).

previous case. A larger relative error, of order 0.5, is obtained in this case, as it can be seen in Fig. 9 and in Fig. 10. However, the trend remains unchanged with respect to the previous case, i.e. we notice a homogeneous relative error for all the ROIs at the lowest thickness of the phantom (1 cm), while, as the thickness increases, the error differentiates between the various ROIs and, in particular, it reaches its maximum value in correspondence of ROI 5; this behavior is expected, since ROI 5 corresponds to 100% of glandular tissue, while ROI 1 is 100% of adipose tissue.

In Fig. 13(b), where the ratio between the scatter-free and the simulated intensities is shown, it is fairly evident that the curves obtained in correspondence of the various thicknesses of the phantom are closer to each other than in case 1 (see Fig. 13(a)), with values ranging from 0.5 to 1.

Case 3. *$[h_S \equiv h_{SG}$ with $SF = 0.2$ and $k = 0.1]$*

In this case, we are considering a Gaussian PSF with about half the amplitude and a standard deviation 10 times higher when compared to case 1. A smaller relative error is obtained, ranging around 0, as reported in Fig. 11 and in Fig. 12. The trend is confirmed to be similar to the previous two cases, but in this circumstance, the relative error, as the thickness of the phantom increases, attains values even equal to -1, in correspondence with the adipose ROI. Therefore, in this case, the intensity values on the scatter-free image are higher than the simulated ones.

In Fig. 13(c) we note that, although the curves related to the various thicknesses are less close to each other than in case 1, they are more symmetrically distributed around the unit value. The general trend, however, remains at values very close to zero for the relative error, and closer to 1 for the ratio plotted in Fig. 13(c); therefore, we can consider the given pair of parameters SF and k satisfactory and a good start point for the following optimization, that will be discussed in the next section.

Case 4. *$[h_S \equiv h_{SH}]$*

Removing the scatter by the hyperbolic PSF h_{SH} defined in (8), we notice a different behavior compared to that one of h_{SG}. In particular, varying SF and k according to Table I, the relative error shows a similar trend in the three cases (additional plots reporting the results obtained varying SF and k according to Table 1 are included in the Supplementary Material, with reference to Fig. S2-S4).

For instance, Figs. 14 and 15 show a relative error close to zero, with values that become strongly negative in ROI 1 (100% of fat tissue) and 2 (75% of fat tissue) for higher thicknesses; moreover, ROIs are distinguishable only at lower thicknesses.

Even looking at the plots in Fig. 13(d), we note very similar trends by varying the parameters SF and k, which confirms a reduced variability when the kernel h_{SH} is exploited (additional plots are included in the Supplementary Material, with reference to Fig. S1-S3).

4. Conclusion

Digital scatter removal is a major challenge in soft tissue imaging and could represent a turning point in clinical practice for better image-based diagnosis, accurate detection of lesions, without affecting the patient dose.

In this paper, a general framework to assess and compare the effectiveness of different methods, based on deconvolution, for digital scatter correction is proposed. To this end, a theoretical model of the image generation process has been defined by taking advantage of a system theory approach. Based on that, some specific research questions to be addressed within the defined theoretical model have been proposed; in particular, the one regarding the estimation of the primary image has been tackled.

To accomplish this goal, the identification of a suitable model of the scatter phenomenon is required; in the case study specifically dealt with in this work, the proposed framework has been applied to compare some of the most widespread methods of scatter correction in mammographic images presented in the literature. In particular, we have focused on two alternative models of the PSF kernel, namely a Gaussian PSF and an hyperbolic PSF as defined by Ducote and Molloi in [26]. Our approach shows encouraging results, with relative error in the range $[-0.5;0.5]$, and allows us to appropriately evaluate digital removal of the scatter, leading to important conclusions on the scatter modeling that depends both on the composition of the tissues and on the thickness of the region of interest, thus laying the foundations for a deeper investigation aimed at improving the scatter correction

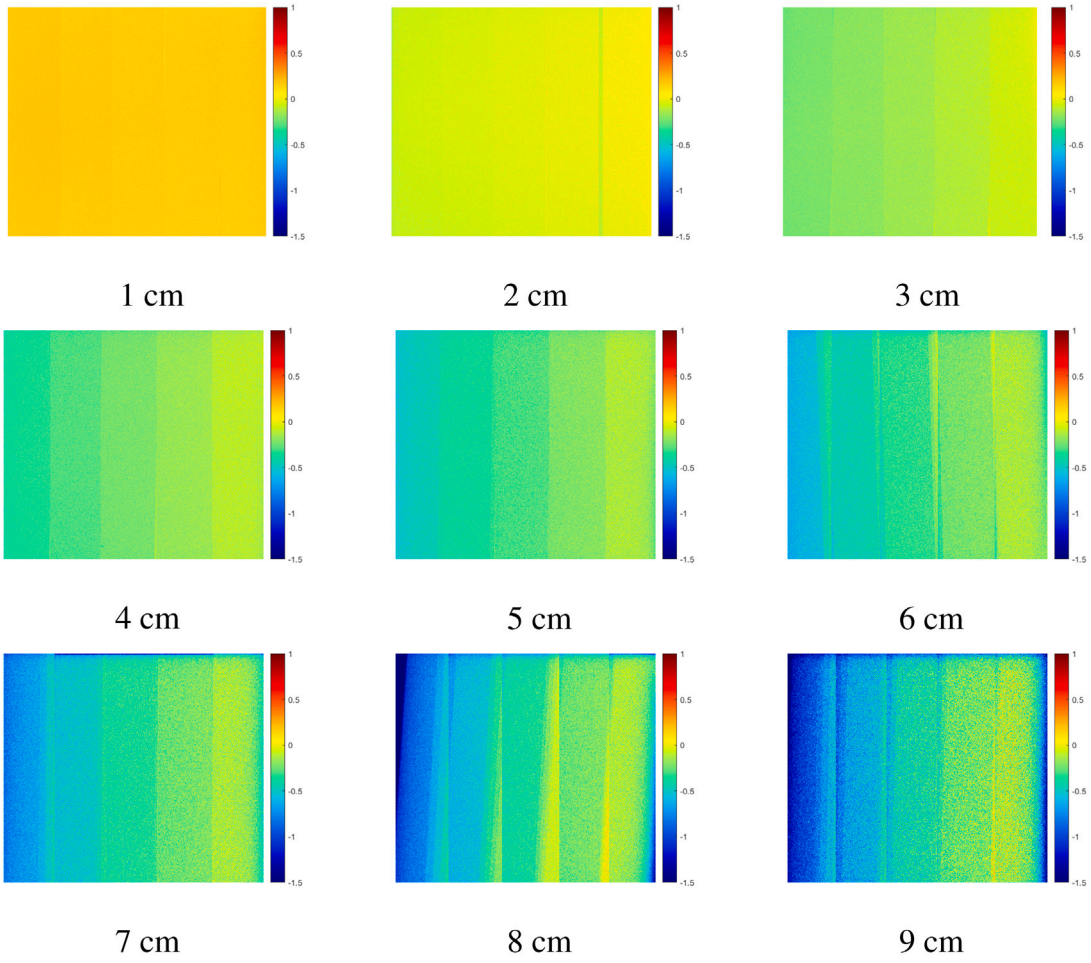

Fig. 14. Relative error distribution on five ROIs of phantom for thickness from 1 cm (top right) to 9 cm (lower left) in case 4.

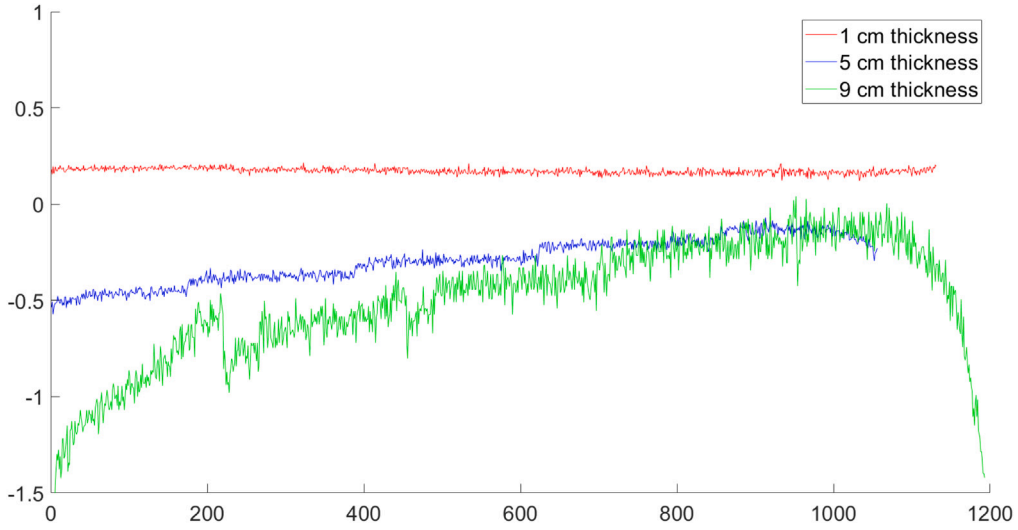

Fig. 15. Relative error trend on five ROIs of phantom for thickness 1 cm, 5 cm and 9 cm in case 4.

algorithms based on the systematic optimization of the parameters modeling the kernel of the image acquisition system. Moreover, the comparison between the two PSF kernels allowed to conclude that a Gaussian kernel performs better than a hyperbolic kernel in reducing the scattering component of the radiation. Several points of interest emerged from the results, which deserve further study. In particular, it is worth noting that the scatter modeling should be optimized based on the composition of the various ROIs and on the thickness of the phantom. In this regard, our study has revealed that, as the thickness of the phantom increases and considering a greater amount of glandular

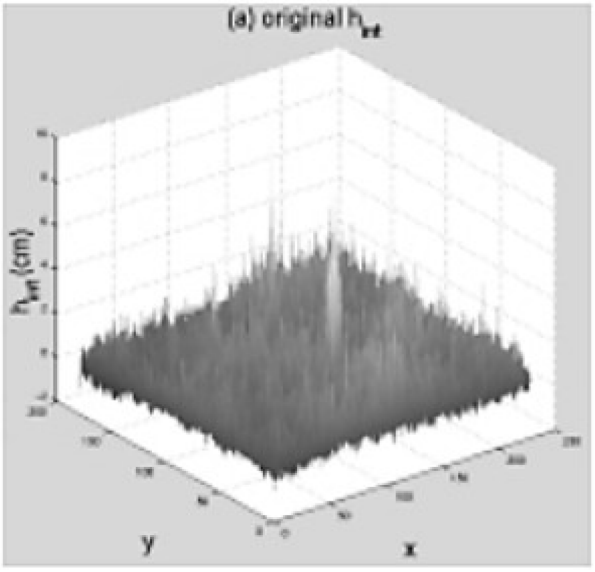

Fig. 16. Surface plot of the original h_{int} of a mammogram sample with a microcalcification.
Source: Reproduced with License n. 5671381318556 from: "Yam, M., Highnam, R., and Brady, M. (1999). De-noising h_{int} surfaces: a physics-based approach. In Medical Image Computing and Computer-Assisted Intervention–MICCAI'99: Second International Conference, Cambridge, UK, September 19–22, 1999. Proceedings 2 (pp. 227–234). Springer Berlin Heidelberg" [37].

tissue inside the ROI, the relative punctual error increases. It can therefore be assumed that SF and k are dependent on both the attenuation coefficient of the tissues and on the thickness of the phantom.

Another interesting point that emerged in our research, is that the variations of the parameters SF and k for the gaussian kernel h_{SG} result in appreciable effects both in the relative error maps and in the plots of the ratio between the scatter-free intensities and the simulated intensities as a function of the ROIs. On the other hand, the hyperbolic kernel h_{SH} is less sensitive to the variations of the parameters and, therefore, is less prone to optimization strategies aimed at adjusting such parameters. As a result, the proper tuning of SF and k for h_{SG} allows a more effective minimization of the error compared to h_{SH}.

As for the limitations and future developments, it should first of all be noted that, having confirmed the feasibility of the same in the case study of the phantom, the application of the proposed framework to the case of a real clinical image requires an initial estimate of the thickness of the glandular tissue and adipose to be able to estimate the theoretical reference model. This has been the subject of previous studies, in particular Highnam and Brady [38] presented an algorithm for estimating h_{int}, assuming only two types of tissue: fat and non-fat. The h_{int} model offers an alternative quantitative representation of the breast tissue, where the h_{int} of a pixel represents the amount of non-fatty breast tissue at that point. An h_{int} representation can be easily visualized as an image, since the h_{int} values are in float format, where brighter parts correspond to regions of the breast with more interesting (non-fatty) tissue. In Fig. 16 is reported a surface plot of the h_{int}. Furthermore, since the proposed framework has been adopted to compare a limited number of PSF kernels, further studies will aim to widen the applications of this approach to different kernels. Moreover, a wider experimental campaign will be conducted to enlarge the dataset, by including images acquired at different settings (varying the X-ray beam properties, KVp and mAs); this will enable a more systematic optimization of the main parameters of the adopted PSF kernels (SF and k). Finally, as the present paper addresses the first one of the research problems described in Section 2.1, in the next papers we will tackle Problem 2, mainly focusing on the identification of the tissue impulse response.

CRediT authorship contribution statement

Francesca Angelone: Formal analysis, Methodology, Validation, Visualization, Writing – original draft, Writing – review & editing, Data curation, Software. **Alfonso Maria Ponsiglione:** Formal analysis, Methodology, Validation, Visualization, Writing – original draft, Writing – review & editing, Data curation, Software. **Roberto Grassi:** Investigation, Project administration, Resources, Writing – review & editing. **Francesco Amato:** Conceptualization, Methodology, Supervision, Writing – review & editing, Investigation, Project administration, Resources. **Mario Sansone:** Conceptualization, Methodology, Supervision, Writing – review & editing, Investigation, Project administration, Resources.

Declaration of competing interest

The authors declare that they have no known competing financial interests or personal relationships that could have appeared to influence the work reported in this paper.

Acknowledgments

This work was carried out as part of a wider project ("Senologia per te") promoted by the Italian Society of Medical Radiology and it was perfomed in collaboration with IMS GIOTTO S.p.A. Sasso Marconi (BO), Italy. The authors warmly thank Valerio Salomone e Angela De Lisio, at IMS, for useful discussions and Jason Holzmann, at Sun Nuclear Corporation, for providing the linear attenuation coefficient of the CESM phantom. All authors have read and approve the manuscript

Appendix A. Supplementary data

Supplementary material related to this article can be found online at https://doi.org/10.1016/j.bspc.2023.105802.

References

[1] C. Dromain, C. Balleyguier, Contrast-enhanced digital mammography, Digit. Mammogr. (2010) 187–198.
[2] F. De Sarno, A.M. Ponsiglione, M. Russo, A.M. Grimaldi, E. Forte, P.A. Netti, E. Torino, Water-mediated nanostructures for enhanced MRI: impact of water dynamics on relaxometric properties of gd-DTPA, Theranostics 9 (6) (2019) 1809.
[3] M. Russo, A.M. Ponsiglione, E. Forte, P.A. Netti, E. Torino, Hydrodenticity to enhance relaxivity of gadolinium-DTPA within crosslinked hyaluronic acid nanoparticles, Nanomedicine 12 (18) (2017) 2199–2210.
[4] F. Arfelli, L. Rigon, R. Menk, Microbubbles as x-ray scattering contrast agents using analyzer-based imaging, Phys. Med. Biol. 55 (6) (2010) 1643.
[5] T. Kretz, K.-R. Müller, T. Schaeffter, C. Elster, Mammography image quality assurance using deep learning, IEEE Trans. Biomed. Eng. 67 (12) (2020) 3317–3326.
[6] L. Donisi, G. Cesarelli, A. Castaldo, D.R. De Lucia, F. Nessuno, G. Spadarella, C. Ricciardi, A combined radiomics and machine learning approach to distinguish clinically significant prostate lesions on a publicly available MRI dataset, J. Imaging 7 (10) (2021) 215.
[7] M. Recenti, C. Ricciardi, K. Edmunds, M.K. Gislason, P. Gargiulo, Machine learning predictive system based upon radiodensitometric distributions from mid-thigh CT images, Eur. J. Transl. Myol. 30 (1) (2020).
[8] M.A. Al-Antari, S.-M. Han, T.-S. Kim, Evaluation of deep learning detection and classification towards computer-aided diagnosis of breast lesions in digital X-ray mammograms, Comput. Methods Programs Biomed. 196 (2020) 105584.
[9] A.M. Ponsiglione, F. Angelone, F. Amato, M. Sansone, A statistical approach to assess the robustness of radiomics features in the discrimination of mammographic lesions, J. Pers. Med. 13 (7) (2023) 1104.
[10] F. Angelone, C. Ricciardi, G. Gatta, M. Sansone, A.M. Ponsiglione, M.P. Belfiore, F. Amato, R. Grassi, Breast density analysis on mammograms: Application of machine learning with textural features, in: 2022 IEEE International Conference on Metrology for Extended Reality, Artificial Intelligence and Neural Engineering (MetroXRAINE), IEEE, 2022, pp. 295–300.
[11] M. Sansone, R. Fusco, F. Grassi, G. Gatta, M.P. Belfiore, F. Angelone, C. Ricciardi, A.M. Ponsiglione, F. Amato, R. Galdiero, et al., Machine learning approaches with textural features to calculate breast density on mammography, Curr. Oncol. 30 (1) (2023) 839–853.

[12] S.Z. Shen, A.K. Bloomquist, G.E. Mawdsley, M.J. Yaffe, I. Elbakri, Effect of scatter and an antiscatter grid on the performance of a slot-scanning digital mammography system, Med. Phys. 33 (4) (2006) 1108–1115.
[13] C.-G. Shaw, D.L. Ergun, P. Myerowitz, M. Van Lysel, C. Mistretta, W. Zarnstorff, A. Crummy, A technique of scatter and glare correction for videodensitometric studies in digital subtraction videoangiography., Radiology 142 (1) (1982) 209–213.
[14] L.A. Love, R.A. Kruger, Scatter estimation for a digital radiographic system using convolution filtering, Med. Phys. 14 (2) (1987) 178–185.
[15] S.Y. Molloi, C.A. Mistretta, Scatter-glare corrections in quantitative dual-energy fluoroscopy, Med. Phys. 15 (3) (1988) 289–297.
[16] S. Naimuddin, B. Hasegawa, C.A. Mistretta, Scatter-glare correction using a convolution algorithm with variable weighting, Med. Phys. 14 (3) (1987) 330–334.
[17] C.E. Floyd, P.T. Beatty, C.E. Ravin, Scatter compensation in digital chest radiography using Fourier deconvolution., Invest. Radiol. 24 (1) (1989) 30–33.
[18] D.G. Kruger, F. Zink, W.W. Peppler, D.L. Ergun, C.A. Mistretta, A regional convolution kernel algorithm for scatter correction in dual-energy images: Comparison to single-kernel algorithms, Med. Phys. 21 (2) (1994) 175–184.
[19] A.H. Baydush, C.E. Floyd Jr., Improved image quality in digital mammography with image processing, Med. Phys. 27 (7) (2000) 1503–1508.
[20] H. Frieser, Spread function and contrast transfer function of photographic layers, Photogr. Sci. Eng. 4 (6) (1960) 324–329.
[21] D.A. Hinshaw, J.T. Dobbins III, Recent progress in noise reduction and scatter correction in dual-energy imaging, in: Medical Imaging 1995: Physics of Medical Imaging, Vol. 2432, SPIE, 1995, pp. 134–142.
[22] A. Ersahin, S. Molloi, Y.-J. Qian, A digital filtration technique for scatter-glare correction based on thickness estimation, IEEE Trans. Med. Imaging 14 (3) (1995) 587–595.
[23] M. Honda, T. Ema, K. Kikuchi, M. Ohe, K.-i. Komatsu, A technique of scatter-glare correction using a digital filtration, Med. Phys. 20 (1) (1993) 59–69.
[24] K.G. Vosburgh, R.K. Swank, J.M. Houston, X-ray image intensifiers, in: Advances in Electronics and Electron Physics, Vol. 43, Elsevier, 1977, pp. 205–244.
[25] J.A. Seibert, O. Nalcioglu, W. Roeck, Characterization of the veiling glare PSF in x-ray image intensified fluoroscopy, Med. Phys. 11 (2) (1984) 172–179.
[26] J. Ducote, S. Molloi, Scatter correction in digital mammography based on image deconvolution, Phys. Med. Biol. 55 (5) (2010) 1295.
[27] M. Sansone, A.M. Ponsiglione, F. Angelone, F. Amato, R. Grassi, Effect of X-ray scatter correction on the estimation of attenuation coefficient in mammography: a simulation study, in: 2022 IEEE International Conference on Metrology for Extended Reality, Artificial Intelligence and Neural Engineering (MetroXRAINE), IEEE, 2022, pp. 323–328.
[28] C. Puett, C. Inscoe, J. Lu, Y. Lee, O. Zhou, Generating synthetic mammograms for stationary 3D mammography, in: Medical Imaging 2019: Physics of Medical Imaging, Vol. 10948, SPIE, 2019, pp. 27–37.
[29] S. Guan, M. Loew, Breast cancer detection using synthetic mammograms from generative adversarial networks in convolutional neural networks, J. Med. Imaging 6 (3) (2019) 031411.
[30] K.H. Cha, N.A. Petrick, A.X. Pezeshk, C.G. Graff, D. Sharma, A. Badal, B. Sahiner, Evaluation of data augmentation via synthetic images for improved breast mass detection on mammograms using deep learning, J. Med. Imaging 7 (1) (2019) 012703.
[31] G. Poludniowski, A. Omar, R. Bujila, P. Andreo, Spekpy v2. 0—a software toolkit for modeling x-ray tube spectra, Med. Phys. 48 (7) (2021) 3630–3637.
[32] K. Kim, W. Kim, S. Kang, D. Lee, H. Cho, G. Kim, S. Park, Y. Lim, C. Park, J. Park, et al., Model-based noise reduction in scatter correction using a deep convolutional neural network for radiography, J. Korean Phys. Soc. 75 (2019) 160–166.
[33] T. Bokulić, B. Vastenhouw, H.W. De Jong, A.J. Van Dongen, P.P. Van Rijk, F.J. Beekman, Monte Carlo-based down-scatter correction of SPECT attenuation maps, Eur. J. Nucl. Med. Mol. Imaging 31 (2004) 1173–1181.
[34] S.M. Leon, L.F. Brateman, L.K. Wagner, Characterization of scatter in digital mammography from physical measurements, Med. Phys. 41 (6Part1) (2014) 061901.
[35] S. Nuclear Corporation, Mammo CESM phantom - QC for contrast enhanced spectral mammography, 2020, Last accessed 15 July 2022, https://www.sunnuclear.com/uploads/documents/datasheets/Diagnostic/CESM_110320.pdf.
[36] G. Richard Hammerstein, D.W. Miller, D.R. White, M. Ellen Masterson, H.Q. Woodard, J.S. Laughlin, Absorbed radiation dose in mammography, Radiology 130 (2) (1979) 485–491.
[37] M. Yam, R. Highnam, M. Brady, De-noising h int surfaces: a physics-based approach, in: Medical Image Computing and Computer-Assisted Intervention–MICCAI'99: Second International Conference, Cambridge, UK, September 19-22, 1999. Proceedings 2, Springer, 1999, pp. 227–234.
[38] R. Highnam, M. Brady, Mammographic Image Analysis, Vol. 14, Springer Science & Business Media, 1999.